Closed-Loop Active Flow Control of a non-steady Flow Field in a Highly-Loaded Compressor Cascade

M. Staats · W. Nitsche · S. J. Steinberg · R. King

Abstract The provision of secure compressor operation under circumstances of a pulsed detonation engine is crucial for the success of pressure gaining combustion processes for turbo machinery applications. This paper discusses Active Flow Control as a possible solution to approach this challenge. The presented experiments were conducted on a highly loaded low speed linear compressor stator cascade. A choking-device which was located in the wake of the cascade simulated the non-steady outflow condition that is expected under the conditions of pressure gaining combustion. The flow structures of the non-steady flow field were strongly correlated to the working-phase of the choking-device. In this paper an Iterative Learning Controller was used to find an optimized actuation trajectory that was used for closed-loop sidewall-actuation to control the corner separation in the non-steady flow field. The Iterative Learning Controller took advantage of the periodicity of the disturbance to calculate a non-steady actuation trajectory that optimally suppressed the impact of the choking-device on the flow. The Active Flow Control effect was evaluated by means of static pressure rise using five hole probe measurements in the wake of one passage.

Keywords Active Flow Control · Linear Compressor Cascade · non-steady Compressor Flow · Iterative Learning Controller

Chair of Aerodynamics
Marchstraße 12
Tel.: +49-30-31421373
Fax: +49-30-31422955
E-mail: marcel.staats@ilr.tu-berlin.de

Chair of Aerodynamics
Marchstraße 12
Tel.: +49-30-31424449
Fax: +49-30-31422955
E-mail: wolfgang.nitsche@tu-berlin.de

Chair of Measurement and Control
Hardenbergstr. 36a
Tel.: +49-30-31423401
Fax: +49-30-31421129
E-mail: simon.steinberg@tu-berlin.de

Chair of Measurement and Control
Hardenbergstr. 36a
Tel.: +49-30-31424100
Fax: +49-30-31421129
E-mail: rudibert.king@tu-berlin.de

1 Introduction

Since the first turbojet powered flight in 1939 many research projects led to major improvements regarding the specific fuel consumption of turbomachinery. By the use of state-of-the-art combustion technology the overall efficiency of single cycle gas turbines is limited to approximately 40%, using the Joule cycle. Nowadays the combustion is an isobaric process, where only minor pressure losses have to be guaranteed to maintain film cooling on the first turbine stator. Multiple research projects are recently aiming for higher overall efficiency of gas turbines. One promising approach to reach efficiency improvements by 10% is to replace the isobaric combustion process by an isochoric one. Benefits of up to 40% fuel savings for a large turbofan engine are stated in [7] and [14]. In [4] an overview about opportunities to improve the thermodynamic cycle of gas turbines is given. It was found that constant volume combustion is always beneficial regarding the engines efficiency. In such an engine the combustion process will be pressure gaining. The combustion can be carried out as pulsed detonations or even more efficient as a shockless explosion combustion. Either way, both combustion concepts are highly non-steady and interact especially with the neighbouring machine parts. The combustion

will be processed using can-annular combustion chambers were the tubes will be closed on the compressor side sequentially when combustion is carried out, in order to keep the disturbances local and manageable, which results in a periodic non-steady outflow condition to the compressor. Especially the compressor stability in all operating points is crucial for the success of the non-steady combustion.

A modern compressor operates with 15 compressor stages to reach the desired overall pressure ratio (OPR) (RR Trent1000: $OPR = 50 : 1$ used in B787). A pulsed detonation engine will still need to be operated with an intermediate pressure compressor to fill the combustion tubes with the required air mass flow. To further reduce the stage count highly loaded stator blades can be used to increase the flow turning and reach higher pressure ratios per stage. Stator blades are referred to as highly loaded, when the de Haller criterion is not fulfilled and the de Haller number drops below $DH = 0.7$.

Increased static pressure ratios can be reached using Active Flow Control (AFC) [3], [12], [24]. An Overview about actuators for Active Flow Control is given in [9]. Looking at compressor stator flows the flow field is dominated by massive three dimensional flow structures and separation phenomena especially at the blade wall junction [17]. The corner separation somehow blocks the passage and limits the operating range of a compressor stator [23], [25]. It can be stated that half of the losses in compressors originate from the end wall region [19]. In [13] pulsed blowing was applied to the end walls and the suction side of the stator blades in a linear cascade, where $8\% - 9\%$ higher static pressure ratios and 13% reduced total pressure losses were reached simultaneously.

In the presented paper results obtained from a linear low speed cascade are shown. The non-steady outflow condition is imposed through a choking-device in the wake of the cascade that blocks every one passage subsequently. It has been shown that the flow field is heavily disturbed under the investigated conditions and Active Flow Control can help to stabilize the flow field [16], [15]. Due to the fact that the choking-device works periodically the occurring flow separation phenomena are periodic as well. Iterative Learning and Repetitive Control was applied to the periodic non-steady flow field, where it was found that the optimal AFC input highly correlates to the working phase of the choking-device [21], [20].

In this contribution an constrained optimization based Iterative Learning Controller was used to find optimal actuation trajectories that were used in closed-loop experiments to control the corner separation of the non-steady operated compressor stator.

2 Experimental Setup

A two dimensional low speed linear compressor stator cascade was used for the investigations. The test rig consisted of seven highly loaded stator blades forming six passages. A choking-device was mounted at $0.71 \cdot c$ behind the trailing edges. Figure 1 shows two dimensional drawings of the test rig and in Table 1 the dimensions of the cascade are listed. The test rig was mounted to a rotatable disk which allowed to adjust the inflow angle from $\alpha = 55°$ to $\alpha = 65°$. In the presented experiments the inflow angle was $\alpha = 60°$. A boundary layer suction was installed to guarantee symmetric inflow conditions to the measurement passage. Adjustable walls and tailboards helped to adjust the desired flow conditions. The inflow conditions where measured through flush mounted static pressure taps at $c/3$ upfront the leading edges and a pitot probe before the nozzle in front of the test rig.

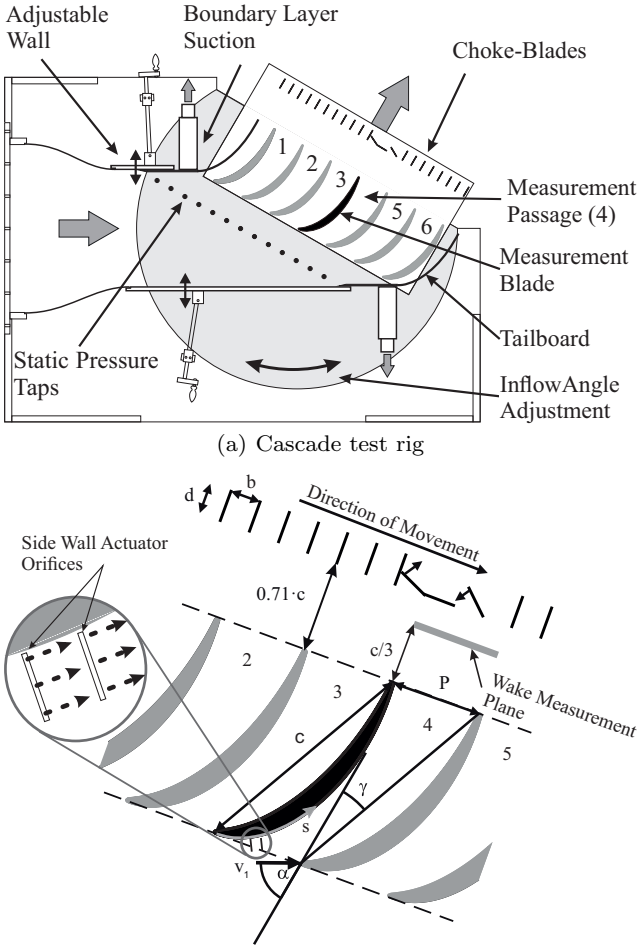

(a) Cascade test rig

(b) Close up of test section

Fig. 1 Experimental setup

Table 1 key data of cascade test rig

Parameter	Value
chord length	$c = 375$mm
blade pitch	$P = 150$mm
blade height	$H = 300$mm
inflow angle	$\alpha = 60°$
stagger angle	$\gamma = 20°$
Mach number	Ma $= 0.07$
Reynolds number	Re $= 600000$
choke-blade height	$d = 50$mm
choke-blade pitch	$b = 50$mm

The wake measurements discussed were evaluated in terms of static pressure rise, that was measured at $c/3$ behind the trailing edges of the measurement passage. Side wall actuation was used for AFC, where only the measurement passage was actuated by one actuator on each end wall with optimized Active Flow Control trajectories and one fixed mass flow actuation set up. The actuators were placed at $s/S = 14.5\%$ relative suction surface coordinate. The devices used for AFC were fluidic actuators that were based on the principle of fluidic amplification as depicted in 2.

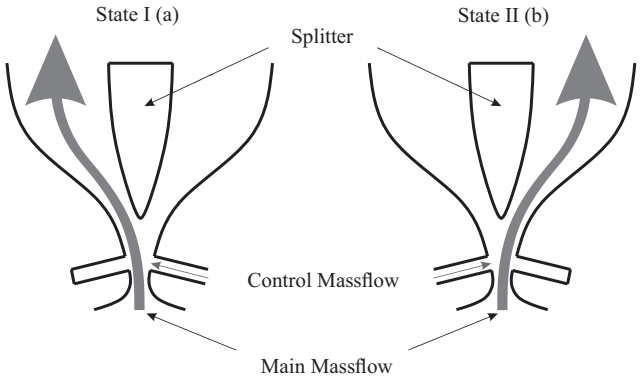

Fig. 2 Actuator principle

Two pneumatic cycles were necessary to operate this actuator. One cycle fed the main mass flow and the second one the control mass flow. Last used 10% to 20% of the main mass flow rate. The actuator operated periodically in two stable states. State one is shown in Figure 2 (a), where the left control port is closed and mass flow was led through the right control port, which caused the power jet to attach on the left wall and the left outlet orifice became active. State two is depicted in Figure 2 (b) and works vice versa. Further information regarding this actuator can be found in [15]. In the presented experiments, the actuator was designed in such way that the two outlet orifices were arranged one after the other in flow direction, with a blowing angle of $\omega = 45°$ as shown in Figure 3. The key measurements of the actuator can be found in this figure as well. The Iterative Learning Controler (ILC) found an optimized actuation trajectory by adjusting the main mass flow. The control mass flow was kept to a constant level at all times. The ILC uses the pressure distribution along midspan of the centre blade of the compressor cascade to find the optimum solution, as it will be described in the next section.

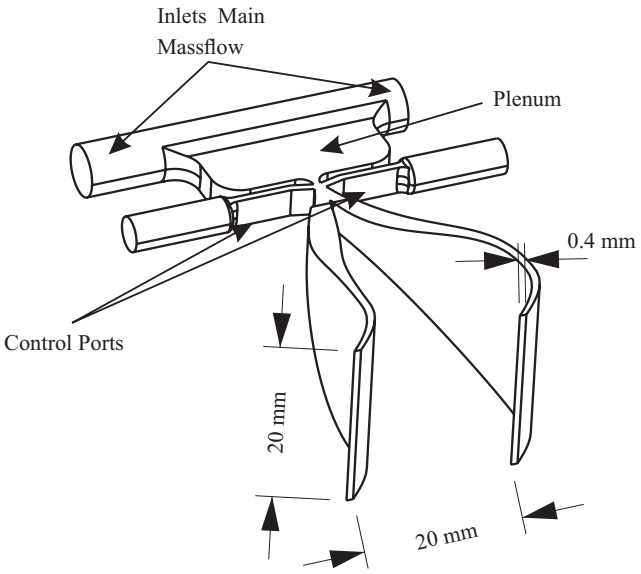

Fig. 3 Side wall actuator

The actuation amplitude is described through the momentum coefficient that is defined as

$$c_\mu = \frac{\dot{m}_{jet} \cdot \bar{u}_{jet}}{q_1 \cdot A_{ref}}, \tag{1}$$

where q_1 is the inflow dynamic pressure and A_{ref} the inflow area of one passage. $\dot{m}_{jet}$ refers to the mass flow of the actuator and $\bar{u}_{jet}$ is the mean actuators output velocity, which is calculated using the actuator geometry and the equation of continuity.

3 Iterative Learning Control

Previous experiments showed that the choking-device induces recurring disturbances in the entire flow field. In a next step, the goal is the mitigation of the impact of these periodic disturbance on the c_p–distribution through a closed–loop active flow control approach. Due to the repetitive nature of the disturbances we decided to implement an Iterative Learning Controller (ILC) [2]. ILCs are specially designed to deal with such repetitive control tasks. By learning from one cycle to the next the

ILC successively improves the actuation trajectory. In this paper, we show results obtained from a constrained optimization–based ILC in its receding–horizon formulation which is based on ideas presented in [10]. After the definition of the input and output variables of the system to be controlled, the lifted system representation [18] is revisited for a general system, and a brief introduction to the learning control algorithm itself is provided.

To avoid any confusion concerning the typography, it should be mentioned that variables primarily related to the field of aerodynamics are presented in the normal font, e.g., x, whereas control theory and signal processing related variables are presented in italic type, e.g., x.

3.1 Definiton of the input and output variables

In the field of control theory dynamic systems are often described by differential equations (continuous–time) or difference equation (discrete–time) that reflect the dynamic input/output behavior of the system to be controlled. In this paper, the input u to the cascade is the amplitude of the sidewall actuators given as the momentum coefficient c_μ. For time step $k \in \mathbb{N}_0$, the input reads as

$$u(k) = \mathrm{c}_\mu(k)\,. \tag{2}$$

The current status of the passage flow is monitored through a surrogate output variable y which is based on the measured midspan $\mathrm{c_p}$–profile of the middle blade's suction surface. For time step k, the output is defined as

$$y(k) = \underline{p}^T\left(\underline{\mathrm{c}}_{\mathrm{p,ref}} - \underline{\mathrm{c}}_\mathrm{p}(k)\right), \tag{3}$$

where $\underline{\mathrm{c}}_\mathrm{p}(k) \in \mathbb{R}^{25}$ is the measured $\mathrm{c_p}$–profile at time step k, $\underline{\mathrm{c}}_{\mathrm{p,ref}} \in \mathbb{R}^{25}$ is the reference $\mathrm{c_p}$–profile describing the case without disturbance and without actuation, and $\underline{p} \in \mathbb{R}^{25}$ with 2-norm $\|\underline{p}\|_2 = 1$ is the *direction* of the $\mathrm{c_p}$–profile that can be manipulated most effectively through the sidewall actuation. A block diagram describing this input/output system is depicted in Figure 4. Equation (3) describes the absolute value of the projection of the current error in the measured $\mathrm{c_p}$–profile onto the direction $\underline{p}$.

The vector $\underline{p}$ is the outcome of a Principal Component Analysis (PCA) [8] which was applied to data obtained from experiments designed to reveal the coherences of actuation amplitude and $\mathrm{c_p}$–profile. In these experiments, the input was varied in a quasi-steady fashion and the resulting change in the $\mathrm{c_p}$–profile was recorded. The PCA then calculates the directions, the so–called principal components, that describe the data best under certain assumptions, for instance, that these directions are orthogonal to each other. For more details please refer to [21], [20], [22].

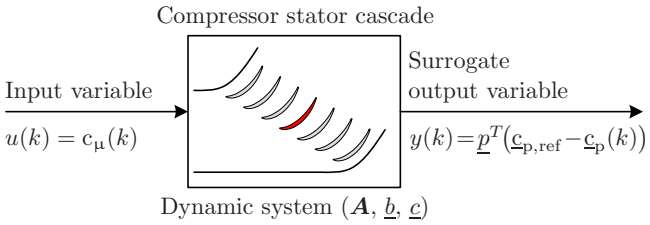

Fig. 4 Definition of system inputs and outputs for the closed–loop controller. The systems dynamic input/output behavior is described by a state space model (4), (5).

In consequence, the surrogate control variable will only detect deviations from the reference if it is possible to mitigate them effectively through the sidewall actuation.

3.2 System description

To introduce the lifted system description, consider a general linear, time–invariant, single–input single–output, discrete–time state space model of the dynamic system to be controlled

$$\underline{x}(k+1) = \boldsymbol{A}\underline{x}(k) + \underline{b}\,u(k)\,,\ \ \underline{x}(0) = \underline{x}_0\,, \tag{4}$$

$$y(k+n_d) = \underline{c}^T\underline{x}(k) + d(k+n_d)\,, \tag{5}$$

where $u(k) \in \mathbb{R}$ is the input, $\underline{x}(k) \in \mathbb{R}^{n_x}$ the state, $y(k) \in \mathbb{R}$ the output, and $d(k) \in \mathbb{R}$ the output disturbance at time step $k \in \mathbb{N}_0$. The output y is assumed to be delayed by $n_d \in \mathbb{N}$ time steps. The relative degree of the system is $\varrho = n_d + 1$. The initial condition is $\underline{x}_0 \in \mathbb{R}^{n_x}$. The first $n_d - 1$ outputs are defined as $y(k) = \underline{c}^T\underline{x}_0 + d(k),\ \forall\ k < n_d$. $\boldsymbol{A} \in \mathbb{R}^{n_x \times n_x}$ is the discrete–time state matrix, $\underline{b} \in \mathbb{R}^{n_x}$ the discrete–time input vector, and $\underline{c} \in \mathbb{R}^{n_x}$ the output vector of the state space model. The system (4), (5) is assumed to be asymptotically stable, observable, and controllable.

Both the reference for the closed–loop operation and the disturbance are assumed to be repetitive, i.e.,

$$r(k) = r(k_i + k)\,, \tag{6}$$

$$d(k) = d(k_i + k)\,, \tag{7}$$

where

$$k_i = i \cdot n_p,\ \forall\, i \in \mathbb{N}_0 \tag{8}$$

defines the point in time from where the i–th cycle, also named iteration, starts and $n_p \in \mathbb{N}$ is the number of time steps per iteration.

A lifted vector describes the time series or the trajectory of its corresponding signal. In this context, the horizon $n_h \in \mathbb{N}$ is the length of the time span that is described by a lifted vector. For causality reasons of the later introduced ILC algorithm, the horizon must be chosen such that $n_h \leq n_p - \varrho$ holds. The lifted input $\boldsymbol{u}(k) \in \mathbb{R}^{n_h}$ and lifted output $\boldsymbol{y}(k) \in \mathbb{R}^{n_h}$ at time step k are defined as

$$\boldsymbol{u}(k) = \begin{cases} \boldsymbol{0} \in \mathbb{R}^{n_h} & , k < n_p - 1 \\ \Big(u(k-n_p+1), \ldots, u(k-n_p+n_h)\Big)^T & , k \geq n_p - 1 \end{cases}, \tag{9}$$

$$\boldsymbol{y}(k) = \begin{cases} \boldsymbol{0} \in \mathbb{R}^{n_h} & , k < n_p - 1 \\ \Big(y(k-n_h+1), \ldots, y(k)\Big)^T & , k \geq n_p - 1 \end{cases}, \tag{10}$$

respectively. The lifted disturbance $\boldsymbol{d}(k)$ and lifted reference $\boldsymbol{r}(k)$ are built up according to (10). The lifted vectors are related to each other via (4) and (5)

$$\boldsymbol{y}(k) = \boldsymbol{G}\boldsymbol{u}(k) + \boldsymbol{F}\underline{x}(k-n_p+1) + \boldsymbol{d}(k)\,, \tag{11}$$

$$\boldsymbol{e}(k) = \boldsymbol{r}(k) - \boldsymbol{y}(k)\,, \tag{12}$$

where $\underline{x}(k-n_p+1)$ is calculated from (4). The matrices $\boldsymbol{G} \in \mathbb{R}^{n_h \times n_h}$ and $\boldsymbol{F} \in \mathbb{R}^{n_h \times n_x}$ read as follows

$$\boldsymbol{G} = \begin{pmatrix} \underline{c}^T\underline{b} & 0 & \ldots & 0 \\ \underline{c}^T\boldsymbol{A}\underline{b} & \underline{c}^T\underline{b} & \ldots & 0 \\ \vdots & \vdots & \ddots & \vdots \\ \underline{c}^T\boldsymbol{A}^{n_h-1}\underline{b} & \underline{c}^T\boldsymbol{A}^{n_h-2}\underline{b} & \ldots & \underline{c}^T\underline{b} \end{pmatrix}, \tag{13}$$

$$\boldsymbol{F} = \Big(\big(\underline{c}^T\boldsymbol{A}\big)^T, \big(\underline{c}^T\boldsymbol{A}^2\big)^T, \ldots, \big(\underline{c}^T\boldsymbol{A}^{n_h}\big)^T\Big)^T. \tag{14}$$

3.3 Constrained optimization–based ILC

The ILC algorithm considered is based on ideas presented in [10]. The ILC solves a time–variant optimization problem in every time step and applies only the first element of the optimal input trajectory to the plant. The ILC uses future predictions of the lifted signal vectors. These predictions are based on measured data from the previous iteration mainly, but are corrected for changes in the initial conditions by a model–based approach.

Let $\hat{\boldsymbol{e}}(k+n_p|k) \in \mathbb{R}^{n_h}$ be the prediction of the future output error $\boldsymbol{e}(k+n_p)$, where information from up to the k–th time step is used to make the prediction. Furthermore, let

$$\hat{\boldsymbol{\mu}}(k+n_p|k) = \hat{\boldsymbol{u}}(k+n_p|k) - \boldsymbol{u}(k) \tag{15}$$

be the change of the *actual past* input trajectory $\boldsymbol{u}(k)$ towards the *predicted future* input trajectory $\hat{\boldsymbol{u}}(k+n_p|k)$. At every time instance k the ILC calculates $\hat{\boldsymbol{\mu}}(k+n_p|k)$ by minimizing the quadratic cost function

$$\begin{aligned} J(k) = \frac{1}{2}\Big(&\hat{\boldsymbol{e}}^T(k+n_p|k)\boldsymbol{W}_e\,\hat{\boldsymbol{e}}(k+n_p|k)\ldots \\ &+ \hat{\boldsymbol{u}}^T(k+n_p|k)\boldsymbol{W}_u\,\hat{\boldsymbol{u}}(k+n_p|k)\ldots \\ &+ \hat{\boldsymbol{\mu}}^T(k+n_p|k)\boldsymbol{W}_\mu\,\hat{\boldsymbol{\mu}}(k+n_p|k)\Big)\,. \end{aligned} \tag{16}$$

The symmetric weighting matrices $\boldsymbol{W}_e \in \mathbb{R}^{n_h \times n_h}$, $\boldsymbol{W}_u \in \mathbb{R}^{n_h \times n_h}$, $\boldsymbol{W}_\mu \in \mathbb{R}^{n_h \times n_h}$ take into account the corresponding lifted vectors. They must be chosen such that the Hessian

$$\boldsymbol{H} = \big(\boldsymbol{G}^T\boldsymbol{W}_e\boldsymbol{G} + \boldsymbol{W}_u + \boldsymbol{W}_\mu\big) \tag{17}$$

is positive definit. Physical limitations, e.g., actuator and state saturations, can be included into the optimization problem by expressing them through a feasible set of $n_m(k) \in \mathbb{N}_0$ inequality constraints and $n_n(k) \in \mathbb{N}_0$ equality constraints

$$\boldsymbol{M}(k)\,\hat{\boldsymbol{\mu}}(k+n_p|k) \leq \underline{m}(k) \tag{18}$$

$$\boldsymbol{N}(k)\,\hat{\boldsymbol{\mu}}(k+n_p|k) = \underline{n}(k) \tag{19}$$

with $\boldsymbol{M}(k) \in \mathbb{R}^{n_m(k) \times n_h}$, $\boldsymbol{N}(k) \in \mathbb{R}^{n_n(k) \times n_h}$, $\underline{m}(k) \in \mathbb{R}^{n_m(k)}$, and $\underline{n}(k) \in \mathbb{R}^{n_n(k)}$.

After some re–arrangements, this optimization problem can be formulated as a standard Quadratic Program (QP) [1]

$$\min_{\hat{\boldsymbol{\mu}}(k+n_p|k)} \frac{1}{2}\,\hat{\boldsymbol{\mu}}(k+n_p|k)^T\boldsymbol{H}\hat{\boldsymbol{\mu}}(k+n_p|k) + \boldsymbol{f}(k)^T\hat{\boldsymbol{\mu}}(k+n_p|k)$$
$$\text{subject to} \begin{cases} \boldsymbol{M}(k)\,\hat{\boldsymbol{\mu}}(k+n_p|k) \leq \underline{m}(k) \\ \boldsymbol{N}(k)\,\hat{\boldsymbol{\mu}}(k+n_p|k) = \underline{n}(k) \end{cases}. \tag{20}$$

Various computationally effective algorithms, e.g., [5], exist to solve (20) in real time. The vector

$$\boldsymbol{f}(k) = -\boldsymbol{G}^T\boldsymbol{W}_e\Big(\boldsymbol{e}(k) - \boldsymbol{F}\Delta\underline{\hat{x}}(k+1)\Big) + \boldsymbol{W}_u\,\boldsymbol{u}(k) \tag{21}$$

contains the measured control errors $\boldsymbol{e}(k)$ and absolute inputs $\boldsymbol{u}(k)$ which represent only data from the current and previous time steps. The term $\boldsymbol{F}\Delta\underline{\hat{x}}(k+1)$ corrects the measured error trajectory $\boldsymbol{e}(k)$ to compensate for iteration-variant initial conditions. The change in the initial condition is based on a simulation approach

$$\Delta\underline{\hat{x}}(k+1) = \begin{cases} \underline{0} \in \mathbb{R}^{n_x} & , k < n_p \\ \boldsymbol{A}\Delta\underline{\hat{x}}(k) + \underline{b}\Big(u(k) - u(k-n_p)\Big) & , k \geq n_p \end{cases}. \tag{22}$$

using the state space model (4).

The optimal $\hat{\boldsymbol{\mu}}(k+n_p|k)$ is obtained from minimizing (20). This allows to calculate $\hat{\boldsymbol{u}}(k+n_p|k)$ through (15). Only the first element of $\hat{\boldsymbol{u}}(k+n_p|k)$ is applied to the

plant at time step k. In the upcoming $(k+1)$–th time step a new optimization problem is solved respecting the new conditions leading to $\hat{\boldsymbol{u}}(k+n_p+1|k+1)$. Repeating this procedure in every time step is referred to as the receding–horizon principle [26].

4 Results

The signal processing and the ILC algorithm were implemented on a `dSPACE` system with a `DS1005` processor board where the QP (20) was solved with `qpOASES` [6]. During the closed–loop experiments, the choking-device ran with a frequency of 2 Hz. The controller sampling time was set to be $T_s = 0.005\,\mathrm{s}$ resulting in a period length of $n_p = 100$ time steps. The parameters of the dynamic model (4), (5) were identified through an experimental approach. To this end, the sidewall actuators excited the passage flow with a Pseudo Random Binary Signal (PRBS) leading to a dynamic response of the cascade. The system response was measured using the surrogate output variable (3). Applying the Prediction Error Method (PEM) [11] to this data leads to a dynamic model. The parameters of the (normalized) model with $n_x = 1$ are

$$\boldsymbol{A} = 0.9386 \quad , \quad \underline{b} = 0.0614 \quad , \quad \underline{c} = 1 \quad , \quad n_d = 3\,. \qquad (23)$$

These model parameters are used within (13) and (14) to built up the system matrices $\boldsymbol{G}$ and $\boldsymbol{F}$, respectively.

For the ILC synthesis, the weighting matrices are chosen to be $\boldsymbol{W}_e = \boldsymbol{I}$, $\boldsymbol{W}_u = 0.25 \cdot \boldsymbol{I}$ and $\boldsymbol{W}_\mu = 10 \cdot \boldsymbol{I}$. Furthermore, three different upper input constraints $\mathrm{c}_{\mu,\max} \in \{0.6\%, 1.0\%, 2.0\%\}$ were considered for the closed–loop experiments. The lower input constraint was set to be $\mathrm{c}_{\mu,\min} = 0.2\%$ to provide the necessary frequency controlling mass flow of the fluidic switches. These physical constraints were implemented by appropriate choices of $\boldsymbol{M}(k)$, $\boldsymbol{N}(k)$, $\underline{m}(k)$, and $\underline{n}(k)$. During the closed–loop experiments, the reference was set to be $\boldsymbol{r} = \boldsymbol{0}$ which expresses the goal to keep the difference $\left(\underline{\mathrm{c}}_{\mathrm{r,ref}} - \underline{\mathrm{c}}_{\mathrm{p}}(t)\right)$ close to zero.

Figure 5, left shows the evolution of the normalized error norm over the iterations for different values of $\mathrm{c}_{\mu,\max}$. Depending on the choice of the controller parameter $\mathrm{c}_{\mu,\max}$, the ILC converges within approximately 10 iterations for the $\mathrm{c}_{\mu,\max} = 0.6\%$ –case and within approximately 45 iterations for the $\mathrm{c}_{\mu,\max} = 2.0\%$ –case. We find that for larger values of $\mathrm{c}_{\mu,\max}$ smaller values of the converged, normalized error norm are achieved. However, the results imply that the actuator is more effective at small actuation amplitudes.

The polar diagram in Figure 5, right, shows the optimal, converged c_μ–trajectories for the different $\mathrm{c}_{\mu,\max}$–cases. It can be seen that the ILC works with very small

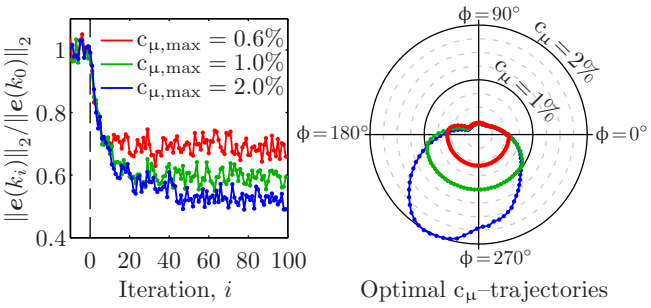

Fig. 5 Left: the evolution of the normalized error norm over the iterations for different values of $\mathrm{c}_{\mu,\max}$. Right: converged, optimal actuation trajectory over the choking-device position ϕ for different values of $\mathrm{c}_{\mu,\max}$.

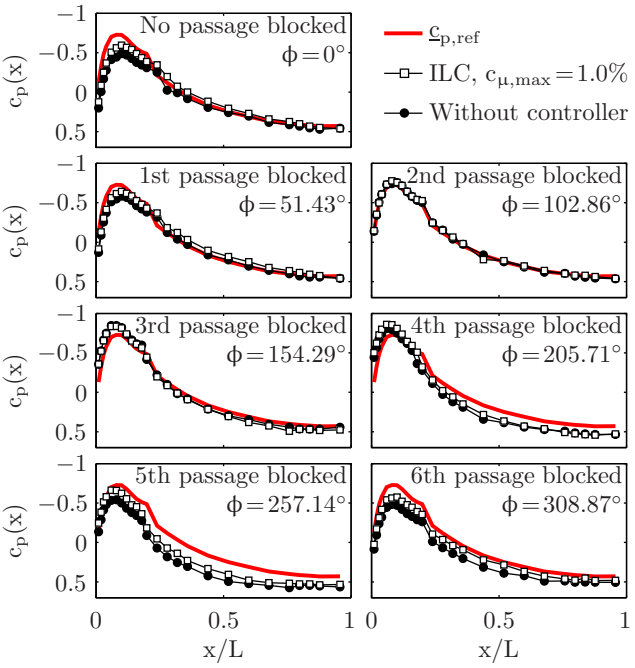

Fig. 6 Time series snapshots of a converged, ILC controlled midspan $\mathrm{c_p}$-profile (□) compared to the case without controller (●). The reference profile $\underline{\mathrm{c}}_{\mathrm{p,ref}}$ (solid, red) represents the case without disturbance and without actuation.

actuation amplitudes around $\mathrm{c}_{\mu,\min}$ for approximately 30% of the cycle. The actuation amplitude is only increased if it is necessary, i.e., if an increase of c_μ leads to a decrease of the cost function (16). We can conclude that utilizing an optimized actuation trajectory has great potential when it comes to saving actuation energy compared to an actuation strategy of constant actuation amplitude.

Figure 6 shows some dedicated snapshots from the time series of a converged, ILC controlled midspan $\mathrm{c_p}$-profile (white, rectangle) compared to the case without controller (black, circle) for the $\mathrm{c}_{\mu,\max} = 1\%$ –case. The reference profile $\underline{\mathrm{c}}_{\mathrm{p,ref}}$ (solid, red) represents the case without disturbance and without actuation. As can be

seen, the controller keeps the profile closer to reference than in the uncontrolled case.

In order to evaluate the performance enhancements due to the actuation, the results of wake measurements are discussed in the following. Therefore, the increment of the static pressure rise coefficient

$$\Delta C_p = C_{p,actu} - C_{p,non-actu}, \tag{24}$$

was used. $C_{p,actu}$ refers to the actuated and $C_{p,non-actu}$ to the non-actuated flow field. The static pressure rise coefficients were measured in the wake of the measurement passage and were calculated using the following equation.

$$C_p = \frac{p_{stat,2} - p_{stat,1}}{q_1} \tag{25}$$

The values $p_{stat,1}$, q_1 were measured in front of the cascade and $p_{stat,2}$ was taken at the wake measurement plane, as depicted in Figure 1(b). The optimal actuation trajectories, found through the ILC, regarded phase dependent mass flow through the actuators. In the experiments the control mass flow of the side wall actuators was fixed to $\dot{m}_{control} = 4.3 \cdot 10^{-4} kg/s$ per actuator and switched, using one solitude valve per actuator with a frequency of $f_{actu} = 60Hz$ in-between the two control ports. The actuator's main mass flow was modulated, which resulted in the specific output behaviour as shown in Figure 7(a), where the dynamic pressure at one output orifice is plotted. With emphasis to the periodic character of the flow field, polar coordinates were chosen. The main mass flow was zero for phase-angles between $\phi = 30°$ to $\phi = 150°$. In these cases only the control mass flow causes the output signal, hence it was constant for the three investigated constrained optimization-based ILC results.

Figure 7(b) depicts the increments in static pressure rise that were phase-averaged and integrated over the whole passage. The three curves $c_{\mu,max} = 0.6\%$, $c_{\mu,max} = 1.0\%$ and $c_{\mu,max} = 2.0\%$ correspond to the optimal solution found through the ILC algorithm. The dashed blue line depicts the result obtained with steady state actuation, where the actuation mass flow was kept constant at $\dot{m} = 10.42 \cdot 10^{-4} kg/s$. This is exactly the average mass flow used in the $c_{\mu,max} = 2.0\%$ case. The actuator's switching frequency was $f_{actu} = 60Hz$ in this case as well. Due to the fact that just the measurement passage is influenced by the side wall actuators, only moderate but still positive increments in static pressure rise occurred with every investigated set of parameters.

Taking the line for the steady state actuation set up in Figure 7(b) into account, it emerges that for

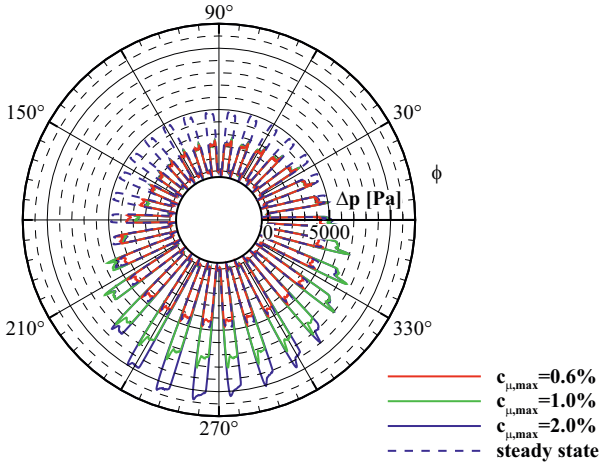

(a) Pressure output signal of one actuator orifice

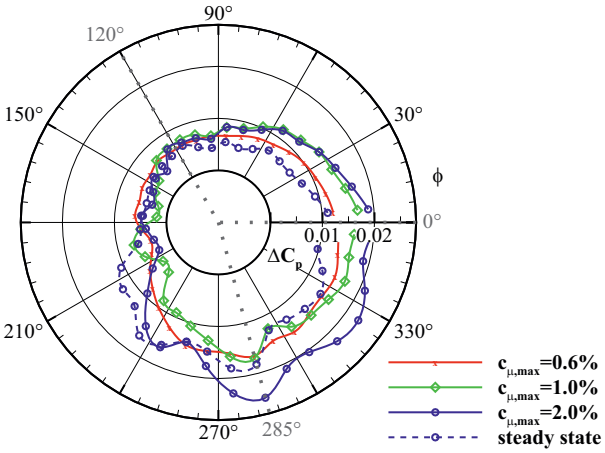

(b) Integral ΔC_p values in the measurement plane

Fig. 7 Actuated Flows

phase-angles $0° < \phi < 90°$ the lowest static pressure rises occurred compared with all other investigated cases. Looking at phase-angles ranging from $90° < \phi < 180°$ indifferent increments in static pressure rises were reached, whereas the pressure output of the actuator had a significant higher amplitude compared to the three other investigated cases. At $180° < \phi < 240°$ a small band of phase-angles was found, where the results of the steady state actuation delivered the highest increase in static pressure rise. In between $240° < \phi < 330°$ the ΔC_p values levelled with the $c_\mu, max = 0.6\%$ and $c_\mu, max = 1.0\%$ cases. In between $330° < \phi < 360°$ the pressure recovery of the passage decreased again and lowest increments in static pressure rise were found in the steady state actuated case.

The phase-dependant modulation of the actuators main mass flow helped to increase the positive effect of the actuation to the static pressure recovery of the

stator passage for a large range of phase-angles. Comparing the actuation amplitudes of the steady state actuation mass flow in Figure 7(a) with the $c_{\mu,max} = 2.0\%$ case, it becomes evident that for phase-angles ranging from $\phi = 10°$ to $\phi = 190°$ these amplitudes were highest for the steady state actuation case. Looking at the remaining phase-angles, mass flow modulated cases had higher amplitudes. Almost identical actuation amplitudes were found for the $c_\mu, max = 0.6\%$ case regarding these phase-angles.

The highest values of ΔC_p are located at phase-angles that do not necessarily correspond to the once with higher actuation amplitudes. Taking phase-angles in-between $0° < \phi < 90°$ into account, it emerges that the curve for the $c_{\mu,max} = 2.0\%$ case converges with the ΔC_p line for the $c_{\mu,max} = 1.0\%$ one at $\phi = 30°$. At $\phi = 90°$ these two curves converge with the $c_{\mu,max} = 0.6\%$ and steady state actuation cases. Comparable ΔC_p results were reached from there on until approaching $\phi = 210°$. The highest increment in static pressure rise was found at $\phi = 285°$ for the $c_{\mu,max} = 2.0\%$ actuation case. Comparing the cases for $c_{\mu,max} = 0.6\%$ and $c_{\mu,max} = 1.0\%$ with each other it showed that comparable static pressure rises were reached when $90° < \phi < 330°$. Leaving this range, higher $\Delta C_p's$ occurred for the $c_{\mu,max} = 1.0\%$.

The detailed passage flow field is shown in Figure 8 regarding three different phase-angles ($\phi = 0°$, $\phi = 120°$, $\phi = 285°$). In this plot, the non-actuated case (Figure 8 (a), (b), (c)) is compared with two actuated ones. In Figure 8 (d), (e), (f) the steady state actuation mass flow was used. For the cases depicted in Figure 8 (g), (h), (i), the optimized actuation trajectory found for $c_{\mu,max} = 2.0\%$ was applied. On the abscissa the relative blade hight coordinate is shown and on the ordinate the relative pitch wise coordinate is plotted. The vector plots depict the off-plane velocity components. In the contour plots the static pressure rises, calculated from (25), become evident. To clearly visualize the position of the corner vortex, the Q-criterion was calculated. In General, the Q-criterion is a common tool to visualize vortex cores in three dimensional and also in two dimensional flows. Positive Q values are an indicator for vortex cores. The dashed line is an iso-Q-line for $Q = 0\frac{1}{s^2}$ and it surrounds areas where $Q > 0\frac{1}{s^2}$ values are found. The Figures 8 (j),(k),(l) show the position of the choking-device that corresponded to the discussed phase-angles.

Taking Figure 8(a) into account, where the phase-angle was $\phi = 0°$, a low pressure region was formed close to the suction sides (ss) wake. This region originated from the strong secondary flow structures forced at the blade-wall junction. In the centre passage moderate static pressure rises were found. As the steady state actuation was switched on, as it is depicted in Figure 8(d), the vector plot significantly changed and a more dominant vortex structure was formed as it can be seen in the vector plot in between $y/H = -0.45$ to $y/H = -0.3$ and $z/P = 0$ to $z/P = 0.3$. Looking at the iso-Q-line, it emerges that the indicated vortex formed closer to the end wall. The side wall actuation had a stabilizing effect to the corner vortex, hence the blockage of the passage was reduced and the static pressure rise was increased. All over the centre passage higher static pressure rises were found compared to Figure 8(a). In Figure 8(g) the optimized actuation trajectory was applied. In this case, the highest static pressure rises were achieved compared to the non-actuated and steady state actuated case. The static pressure inside the area surrounded by the iso-Q-line is also higher compared to the steady-state actuation. In both actuated cases the effect of the actuation to the shape of the corner vortex is similar.

When the phase-angle $\phi = 120°$ was investigated as it is shown in Figure 8(b), 8(e) and 8(h) the static pressure rises were lower in contrast to the related cases for the phase-angle $\phi = 0°$. At this phase-angle the blade experienced a very high aerodynamic loading, which forced the trailing edge separation to become larger, hence static pressure rises were limited. Figure 8(b) shows a large area of low static pressure rises starting at $z/P = 0.1$ and reaching up to $z/P = 0.6$. The highest static pressure rises were still found at the end-wall region in the centre passage. Due to the larger trailing edge separation the vortex indicated through the Q-criterion was shifted in pitch wise direction, further into the passage. Regarding the actuated cases, it became apparent that for this phase-angle the effect actuation had to the integral static pressure rise was independent from the actuation trajectory, that was used in the experiments. Still, there are some differences found in the detailed flow fields data. Taking Figure 8(e) with steady state actuation into account, it was found that the isolated region of low static pressure rises was significantly smaller as was the area encircled by the iso-Q-line. Comparing this state with the case shown in Figure 8(h), where the optimized actuation trajectory was applied, it is found that the higher actuation mass flow used in the Figure 8(e) forces a regions of very low pressure rises ranging from $y/H = -0.4$ to $y/H = -0.3$ and $z/P = 0.2$ to $z/P = 0.4$, that was not found in Figure 8(h).

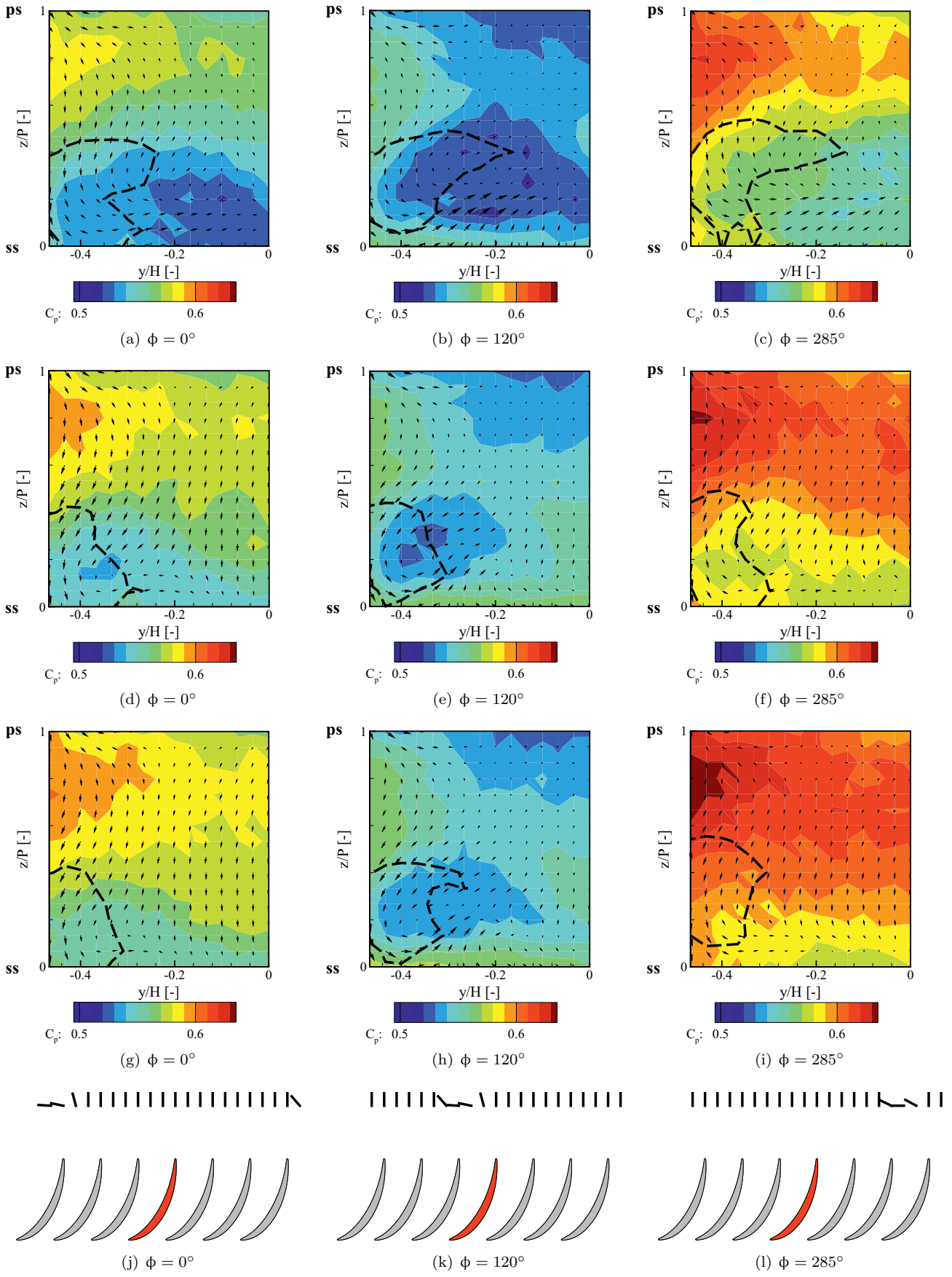

Fig. 8 Static pressure rises (C_p) for different phase-angles; non-actuated case (a,b,c); steady state mass flow actuation (d,e,f); optimal actuation trajectory for $c_{\mu,max} = 2.0\%$ (g,h,i)

The lower actuation mass flow used in the optimized case in Figure 8(h) caused the corner vortex to be larger as it is seen by the iso-Q-line. But in this certain case the higher mass flow does not influence the flow field in a more effective way.

Taking the phase-angle $\phi = 285°$ into account, generally the highest static pressure rises were found. The non-actuated case showed a large area of static pressure coefficients with $C_p >= 0.6$ in the centre passage. At pitch wise positions of $z/P <= 0.6$ lower static pressure occurred. The iso-Q-line reaches the most into the passage compared to the two other phase-angles discussed. In this case, the secondary flow originating from the corner separation spreads out the most over the passage and it's actuation promises the most positive effect. As depicted in Figure 7(b), the highest increments in static pressure rise was found at this specific phase-angle regarding all actuated cases. Figure 8(f) shows the flow field as it developed for the steady state actuated case at the phase-angle $\phi = 285°$. Again the dimension of the area surrounded by $Q = 0\frac{1}{s^2}$ became smaller due to the actuation. In the centre passage a more homogeneous pressure field forms. When the optimized actuation trajectory was applied, as it is shown in Figure 8(i), the core of the corner vortex was shifted pitch wise towards higher z/P values. A very uniform pressure distribution developed between $z/P = 0.4$ until the end of the passage at $z/P = 1$. At coordinates close to the wake of the measurement blade a low pressure region forms, which could not be influenced by the side-wall actuators.

5 Conclusions

In the presented paper a compressor stator flow was discussed, in which a two dimensional low speed compressor cascade was operated under highly non-steady conditions that would be expected under the regime of a pulsed detonation engine. The non-steady outflow condition was imposed by a choking-device situated in the wake of the seven blades, causing a periodical choking of every one passage. Due to the fact that the disturbances were periodic, a constrained optimization based Iterative Learning Controller was used to modulate the input of two side wall actuators situated in the measurement passage to control the corner separation in this one passage. The static pressure distribution along the blade at midspan was used to calculate the output variable the ILC used. Wake measurements gave evidence about the effectiveness of the optimized actuation trajectories. The results were compared to a steady state actuation trajectory, which showed that the mass flow modulated actuator output helped to affect the corner separation more effectively in terms of static pressure rise in contrast to the steady state actuation trajectory. Local increments in static pressure rise of $\Delta C_p = 2.5\%$ were reached, where the steady state actuation only reached $\Delta C_p = 1.9\%$. The experiments showed that the chosen approach in the ILC algorithm led to positive effects regarding the compressor performance in terms of static pressure rise.

Acknowledgements The authors gratefully acknowledge support by the Deutsche Forschungsgemeinschaft (DFG) as part of collaborative research center SFB 1029 "Substantial efficiency increase in gas turbines through direct use of coupled unsteady combustion and flow dynamics".

References

1. Boyd, S., Vandenberghe, L.: Convex Optimization. Cambridge University Press (2004)
2. Bristow, D., Tharayil, M., Alleyne, A.: A survey of iterative learning control. IEEE Control Systems **26**(3), 96–114 (2006). DOI 10.1109/MCS.2006.1636313
3. D. Nerger and H. Saathoff and R. Radespiel and V. Gümmer and C. Clemen: Experimental Investigation of Endwall and Suction Side Blowing in a Highly Loaded Compressor Stator Cascade. Journal of Turbomachinery **134** (2012)
4. F. Schmidt and S. Staudacher: Generalized Thermodynamic Assessment of Concepts for Increasing the Efficiency of Civil Aircraft Propulsion Systems. Proceedings of ASME Turbo Expo 2015: Turbine Technichal Conference and Exposition GT2015 (2015)
5. Ferreau, H., Bock, H., Diehl, M.: An online active set strategy to overcome the limitations of explicit MPC. International Journal of Robust and Nonlinear Control **18**(8), 816–830 (2008)
6. Ferreau, H., Kirches, C., Potschka, A., Bock, H., Diehl, M.: qpOASES: A parametric active-set algorithm for quadratic programming. Mathematical Programming Computation **6**(4), 327–363 (2014). DOI DOI 10.1007/s12532-014-0071-1
7. G. Lenoble and S. Ogaji: Performance analysis and optimization of a gas turbine cycle integrated with an internal combustion wave rotor. Proceedings of the Institution of Mechanical Engineers, Part A: Journal of Power and Energy **224**(7), 889–900 (2010)
8. Jackson, J.E.: A User's Guide to Principal Components. John Wiley & Sons, New York (1991)
9. L. N. Cattafesta III and M. Sheplak: Actuators for Active and Flow Control. Annu. Rev. Fluid Mech. **43**, 247–272 (2011)
10. Lee, J., Natarajan, S., Lee, K.: A model-based predictive control approach to repetitive control of continuous processes with periodic operations. Journal of Process Control **11**(2), 195 – 207 (2001)
11. Ljung, L.: System Identification: Theory for the User (2nd Edition). Prentice Hall, Englewood Cliffs, New Jersey (1999)
12. M. Hecklau and C. Gmelin and W. Nitsche and F. Thiele and A. Huppertz and M. Swoboda: Experimental and numerical results of active flow control on a highly loaded stator cascade. Proceedings of the Institution of Mechanical Engineers, Part A: Journal of Power and Energy **225**, 907–918 (2011)

13. M. Hecklau and V. Zander and I. Peltzer and W. Nitsche and A. Huppertz and M. Swoboda: Experimental AFC Approaches on a Highly Loaded Compressor Cascade. In: King, R. (ed.) Active Flow Control II, *Notes on Numerical Fluid Mechanics and Multidisciplinary Design*, vol. 108, pp. 171–186. Springer Berlin Heidelberg (2010)
14. M. R. Nalim and H. Li and P. Akbari: Air-Standard Aerothermodynamic Analysis of Gas Turbine Engines With Wave Rotor Combustion. Journal of Engineering for Gas Turbines and Power **131**(5), 054,506 (2009)
15. M. Staats and W. Nitsche: Active Control of the Corner Separation on a Highly Loaded Compressor Cascade with Periodic Non-Steady Boundary Conditions by means of Fluidic Actuators. Proceedings of the ASME Turbo Expo 2015, June 15-18, Montreal, Canada, ASME paper GT2015-42161 (2015)
16. M. Staats and W. Nitsche and I. Peltzer: Active Flow Control on a Highly Loaded Compressor Cascade with Non-Steady Boundary Conditions. In: King, R. (ed.) Active Flow and Combustion Control 2014, *Notes on Numerical Fluid Mechanics and Multidisciplinary Design*, vol. 127, pp. 23–37. Springer International Publishing (2015)
17. N. A. Cumpsty and E. M. Greitzer: Ideas and methods of turbomachinery aerodynamics: a historical view. Journal of propulsion and power **20**(1), 15–26 (2004)
18. Phan, M., Longman, R.: A mathematical theory of learning control for linear discrete multivariable systems. In: Proceedings of the AIAA/AAS Astrodynamics Conference, Minneapolis, USA, August (1988)
19. S. A. Khalid and A. S. Khalsa and I. A. Waitz and C. S. Tan and E. M. Greitzern and N. A. Cumpsty and J. J. Adamczyk and F. E. Marble: Endwall blockage in axial compressors. In: ASME 1998 International Gas Turbine and Aeroengine Congress and Exhibition, pp. V001T01A047–V001T01A047. American Society of Mechanical Engineers (1998)
20. S J. Steinberg and M. Staats and W. Nitsche and R. King: Iterative Learning Active Flow Control Applied to a Compressor Stator Cascade With Periodic Disturbances. Proceedings of ASME Turbo Expo 2015: Turbine Technical Conference and Exposition GT2015 (2015)
21. Steinberg, S., Staats, M., Nitsche, W., King, R.: Comparison of Iterative Learning and Repetitive Control Applied to a Compressor Stator Cascade. In: King, R. (ed.) Active Flow and Combustion Control 2014, *Notes on Numerical Fluid Mechanics and Multidisciplinary Design*, vol. 127, pp. 39–53. Springer International Publishing (2015)
22. Steinberg, S., Tiedemann, C., King, R., Peitsch, D.: Identification of surrogate control variables for a robust active flow controller of an experimental high speed stator cascade. In: Proceedings of the ASME Turbo Expo 2013, June 3-7, San Antonio, Texas, USA, GT2013-94179, vol. 4 (2013). DOI 10.1115/GT2013-94179
23. V.-M. Lei and Z. S. Spakovszky and E. M. Greitzer: A criterion for axial compressor hub-corner stall. Journal of Turbomachinery **130**(3), 031,006 (2008)
24. V. Zander and M. Hecklau and W. Nitsche and A. Huppertz and M. Swoboda: Active Flow Control by Means of Synthetic Jets On a Highly Loaded Compressor Cascade. Proceeedings of the Institution of Mechanical Engineers, Part A: Journal of Power and Energy **225**, 897–906 (2011)
25. W. Ma and X. Ottavy and L. Lu and F. Leboeuf and F. Gao: Experimental Study of Corner Stall in a Linear Compressor Cascade. Chinese Journal of Aeronautics **24**, 235–242 (2011)
26. Wang, L.: Model Predictive Control System Design and Implementation Using MATLAB. Advances in Industrial Control. Springer, London (2009). DOI 10.1007/978-1-84882-331-0